frontiers | Frontiers in Bioengineering and Biotechnology

ORIGINAL RESEARCH
published: 19 July 2022
doi: 10.3389/fbioe.2022.915702

Design of an Integrated Microvascularized Human Skin-on-a-Chip Tissue Equivalent Model

Christian F. E. Jones[1,2], *Stefania Di Cio*[1,2], *John T. Connelly*[3] *and Julien E. Gautrot*[1,2]*

[1]*Institute of Bioengineering, Queen Mary University of London, London, United Kingdom,* [2]*School of Engineering and Materials Science, Queen Mary University of London, London, United Kingdom,* [3]*The Blizard Institute, Queen Mary University of London, London, United Kingdom*

OPEN ACCESS

Edited by:
Ratima Suntornnond, Nanyang Technological University, Singapore

Reviewed by:
Surasak Kasetsirikul, Griffith University, Australia
Pei Zhuang, Harvard Medical School, United States

***Correspondence:**
Julien E. Gautrot
j.gautrot@qmul.ac.uk

Specialty section:
This article was submitted to Biomaterials, a section of the journal Frontiers in Bioengineering and Biotechnology

Received: *08 April 2022*
Accepted: *09 May 2022*
Published: *19 July 2022*

Citation:
Jones CFE, Di Cio S, Connelly JT and Gautrot JE (2022) Design of an Integrated Microvascularized Human Skin-on-a-Chip Tissue Equivalent Model. Front. Bioeng. Biotechnol. 10:915702. doi: 10.3389/fbioe.2022.915702

Tissue-engineered skin constructs have been under development since the 1980s as a replacement for human skin tissues and animal models for therapeutics and cosmetic testing. These have evolved from simple single-cell assays to increasingly complex models with integrated dermal equivalents and multiple cell types including a dermis, epidermis, and vasculature. The development of micro-engineered platforms and biomaterials has enabled scientists to better recreate and capture the tissue microenvironment *in vitro*, including the vascularization of tissue models and their integration into microfluidic chips. However, to date, microvascularized human skin equivalents in a microfluidic context have not been reported. Here, we present the design of a novel skin-on-a-chip model integrating human-derived primary and immortalized cells in a full-thickness skin equivalent. The model is housed in a microfluidic device, in which a microvasculature was previously established. We characterize the impact of our chip design on the quality of the microvascular networks formed and evidence that this enables the formation of more homogenous networks. We developed a methodology to harvest tissues from embedded chips, after 14 days of culture, and characterize the impact of culture conditions and vascularization (including with pericyte co-cultures) on the stratification of the epidermis in the resulting skin equivalents. Our results indicate that vascularization enhances stratification and differentiation (thickness, architecture, and expression of terminal differentiation markers such as involucrin and transglutaminase 1), allowing the formation of more mature skin equivalents in microfluidic chips. The skin-on-a-chip tissue equivalents developed, because of their realistic microvasculature, may find applications for testing efficacy and safety of therapeutics delivered systemically, in a human context.

Keywords: organ-on-a-chip, skin, microfluidic, microvasculature, organotypic, keratinocyte, endothelial cell, pericyte

1 INTRODUCTION

Our ability to recreate a more complex tissue structure and function has considerably improved. As the fields of micro-engineering and biomaterial science developed, it has become increasingly clear that recreating some of the 3D architectures of tissues may be essential to reproduce the cell microenvironment and direct cell phenotype and tissue structure or function. Dating back to the 80s, micro-engineered platforms allowed the control of single-cell adhesion and patterning, in turn allowing to control their phenotype (Watt et al., 1988; Chen et al., 1997; Connelly et al., 2010; Tan et al., 2013). More recently, the formation of clusters allowing to capture more complex behaviors, including cell segregation, motility, sprouting, and differentiation have been developed (Nelson et al., 2006; Ruiz and Chen, 2008; Gautrot et al., 2012; Costa et al., 2014). However, these platforms remained inherently based on 2D models, certainly relevant to cells forming 2D assemblies such as epithelia, but clearly limiting the creation of more complex architectures. Although interesting strategies were proposed to bridge the 2D and 3D worlds (Bosch-Fortea et al., 2019), making use of 2D patterns to guide cell assembly in a 3D matrix, our ability to micro-engineer 3D tissues required the development of novel platforms.

The field of skin biology was certainly the first to see striking progress in the development of complex hierarchical tissue structures, with stratified differentiated skin equivalents of human tissues formed from epidermal keratinocytes assembling as monolayers at the surface of hydrogels encapsulating fibroblasts (Shahabeddin et al., 1990; Stark et al., 2006). This allowed not only the recreation of well-differentiated human skin equivalents but also allowed capturing of some of the skin barrier functions, from trans-epithelial resistance to the diffusion of therapeutics and nanomaterials (Asbill et al., 2000; Mazlyzam et al., 2007; Ackermann et al., 2010; Bellas et al., 2012). These include models which have integrated other *in vivo* skin structures and cell types including the hair follicle (Langan et al., 2015) and melanocytes (Liu et al., 2007; Li et al., 2011). More recently, a broad range of tissues has beneficiated from advances in stem cell biology, spheroid, and organoid models and progress in biomaterials and microfabrication. This ranges from the formation of functional muscles and lung tissue models (Huh et al., 2010; Sakar et al., 2016; Ronaldson-Bouchard et al., 2018) to the development of complex organoid models, for example, of gut, skin, and brain tissues (Lancaster et al., 2013; Lee et al., 2020).

As tissues grew in complexity and size, vascularization became an important hurdle, either to their further development or growth, or simply their long term survival and applicability (Colton, 1995; Coloma et al., 1997; Baish et al., 2011). In addition, recapitulating the complex architecture and function of microvascularized tissues will be important for the accurate prediction of therapeutic safety and efficacy (Loskill et al., 2021), for example, mimicking systemic delivery to targeted tissues. To address this issue, a range of tissue models have been placed in parallel with endothelialized structures, therefore allowing to recreate the endothelium-tissue interface. This has, in particular, been exploited in a broad range of tissue-on-chip models, using porous membranes to separate an endothelial compartment from a tissue compartment (Huh et al., 2010; Kim and Ingber, 2013; Kilic et al., 2016; Hassell et al., 2017). In addition to simply structuring tissues, this approach enables the mechanical stimulation of resulting tissues, an important factor regulating cell and tissue biology and response to pathogens or during disease progression. To recreate more functional models of vessels, a range of platforms have been engineered to allow the endothelialization of micro-capillaries and microchannels, allowing to study phenomena such as sprouting and angiogenesis in more realistic scenarios (Menon et al., 2017; Trappmann et al., 2017; Liu et al., 2021).

Increasingly, microvascularized models have become popular, enabling to accurately capture the architecture and function of microvascular networks perfusing tissues (Polacheck et al., 2014). An early work from Kamm et al. and Jeon et al.(2015) showed that microvascular networks can conveniently be assembled and maintained in microfluidic chips, allowing the formation of perfusable capillaries (Kim et al., 2013; Galie et al., 2014). Such models can be derived through angiogenesis, from endothelialized microchannel interfaces with hydrogel compartments separated by micro-posts, or by the direct assembly of networks *via* vasculogenesis, therefore enabling the faster formation of functional structures. Subsequently, hydrogel compartments were loaded with stem cells and disease cell lines to recreate vascularized tissue models (Kim et al., 2015a; Jeon et al., 2015; Chen et al., 2017). Another attractive alternative proposed consists of placing spheroids, and in some cases, organoids within wells designed within the hydrogel compartment, therefore enabling the vascularization of the resulting tissue models (Sobrino et al., 2016; Ko et al., 2019a; Homan et al., 2019; Shin et al., 2021). Although this remains moderately successful for the interpenetration of organoids, this strategy has been particularly promising for spheroid models.

The field of skin biology has seen the development of a range of skin equivalents interfaced with endothelial models. For example, endothelial barriers were formed at the bottom or back of the dermal compartments of human skin equivalents (Wufuer et al., 2016; Lee et al., 2017; Kwak et al., 2020) including in microfluidic chips, and micro-capillaries were allowed to assemble at the bottom of the dermal constructs in transwell systems (Black et al., 1998; Black et al., 1999). Such models of skin vascularization displayed an improved epidermal barrier function (Kim et al., 2019; Kwak et al., 2020) and basal cell proliferation and differentiation (Kim et al., 2019), compared with non-endothelialized equivalents. However, few successful vascularized skin-equivalent models, integrated into microfluidic chips, have been reported to date.

In this report, we present the design of a full-thickness human skin-on-a-chip model displaying a stratified differentiated epidermal compartment, assembled above a microvascularized dermal compartment (**Figure 1**). We first design a novel microfluidic chip featuring a circular central chamber separated from circumferential channels by micro-posts and characterize the impact of such a structure on the morphology of the microvasculature. We then identify culture conditions suitable for the formation of a stratified human skin equivalent in the resulting chips, before evaluating the impact

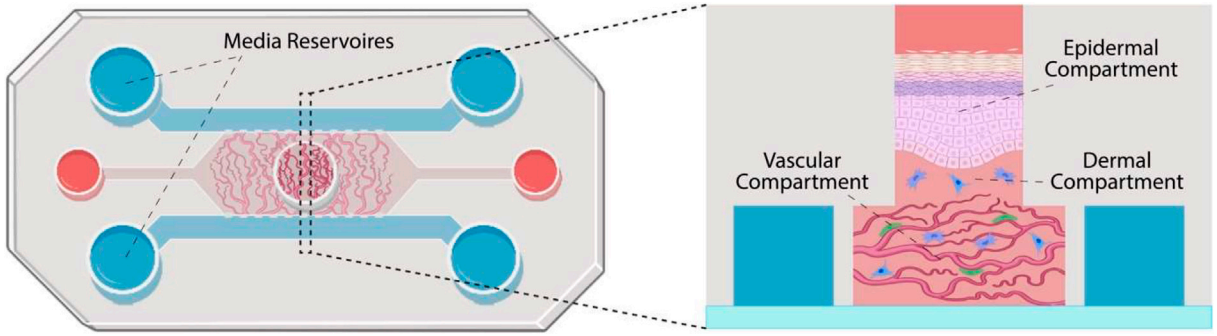

FIGURE 1 | Schematic representation of the skin-on-a-chip model proposed. The chip is constituted of three parallel channels separated by micro-posts and connecting media reservoirs. A central well is positioned in the center of the central channel. The vascular compartment is formed in the central channel (microvasculature shown in red and pericytes in green). Dermal fibroblasts (in blue) are introduced within a second hydrogel compartment, in the central well, before keratinocytes are seeded and allowed to stratify (in pink).

of vascularization on the resulting tissue structure and epidermal differentiation. In addition, we introduce pericytes in the vascular compartment, to stabilize associated structures and evaluate the impact of such a co-culture on the resulting vascularized skin equivalents. Overall, our results demonstrate the formation of vascularized skin-on-chip models that could be scaled and parallelized to design high throughput platforms for the testing of the safety and efficacy of therapeutics.

2 MATERIALS AND METHODS

2.1 Chip Design and Manufacture

Chips were designed in AutoCAD by AutoDesk and printed on acetate sheets by Micro Lithography Services, Chelmsford, United Kingdom. The design selected is based on three channel chips (**Figures 1** and **Figures, 2A,B**) in which three parallel linear channels are separated by micro-posts (hexagonal posts, 380 µm long and 90 µm wide). Central chambers (hexagonal or circular, 5 mm wide) were introduced to allow 1 mm gaps on either side of an integrated 3-mm diameter circular central well open to the air.

Microfluidic chips were generated using Sylgard™ 184 PDMS and glass coverslips, following the literature protocols (Jenkins, 2013). In short, masters were manufactured by coating clean silicon wafers with a negative photoresist (SU-2050) using a spin coater set to 500 rpm for 10 s (ramp 100 rpm/s for the initial 5 s) to distribute the photoresist, followed by a spin speed of 1,700 rpm for 30 s (ramp 300 rpm/s for the initial 4 s) to spread the resist to a uniform depth of 80 µm. After an initial soft bake at 65°C for 3 min and then at 95°C for 10 min to harden the surface of the photoresist, photomasks corresponding to the desired chip micro-architectures were placed on the surface of the wafer and photocured with UV light at 90 mW/cm^2 for 2.4 s, allowing resist crosslinking to occur. The resists were post-baked at 65°C for 3 min and then at 95°C for 10 min to assist the crosslinking, allowing to rest in between, then immersed in propylene glycol methyl ether acetate (PGMEA, Sigma Aldrich, 484431) for 5 min to dissolve un-crosslinked photoresists. The masters were immediately rinsed with isopropanol to remove excess PGMEA and dried under a stream of nitrogen. The resulting masters were examined using a reflected light microscope to confirm suitable patterning and then incubated at 150°C for 3 min to hard bake the photoresist. The PDMS base (Sylgard™ 184) was mixed with its curing agent at a 10:1 ratio, after which air bubbles were removed *via* centrifugation or under vacuum. The resulting formulation was poured onto the masters to a depth of 5 mm, placed under vacuum again to eliminate bubbles, and then left overnight at 70°C to allow full curing. The PDMS blocks were cut away from the masters to produce a stamp with features corresponding to the microarchitecture of the master. Biopsy punches were used to introduce cell culture medium reservoirs and hydrogel inlets, which can then be cleaned with residue-free tape to remove any obvious debris and rinsed with deionized water and isopropanol or ethanol before drying in nitrogen. The stamps were placed in an air plasma system (HPT-200, Henniker Plasma) and treated for 1 min with the channels facing upward, alongside glass coverslips. The PDMS blocks were then rapidly pushed firmly against the coverslip for 30 s to allow bonding and each chip was carefully inspected to ensure the system was fully sealed. Finally, the chips were autoclaved and left in an oven for at least 48 h to allow the PDMS to recover its hydrophobicity.

2.2 Cell Culture

All primary cells used as part of this project were between passage numbers 3–6. Cells were cultured in T75 Nunc™ EasYFlask™ cell culture flasks (Thermo Fisher®, 156499) at 37°C and 5% CO_2 and passaged at approximately 80% confluency. HUVECs were obtained from Lonza™ and cultured in Endothelial Cell Growth Medium-2 (EGM-2, PromoCell® C-22111 or Lonza™ CC-3162). Human primary pericytes were purchased from PromoCell® (PromoCell®, C-12980) and cultured in Pericyte Growth Medium-2 (PGM2), also from PromoCell® (PromoCell®, C-28041). Detachment was achieved using a pericyte detachment kit (PromoCell®, C-41200), requiring the addition of 5 ml HEPES buffered saline solution to the cells for washing, after medium aspiration, aspiration, and the addition of 5 ml Trypsin/EDTA 0.04%/0.03% for 3 min at room temperature.

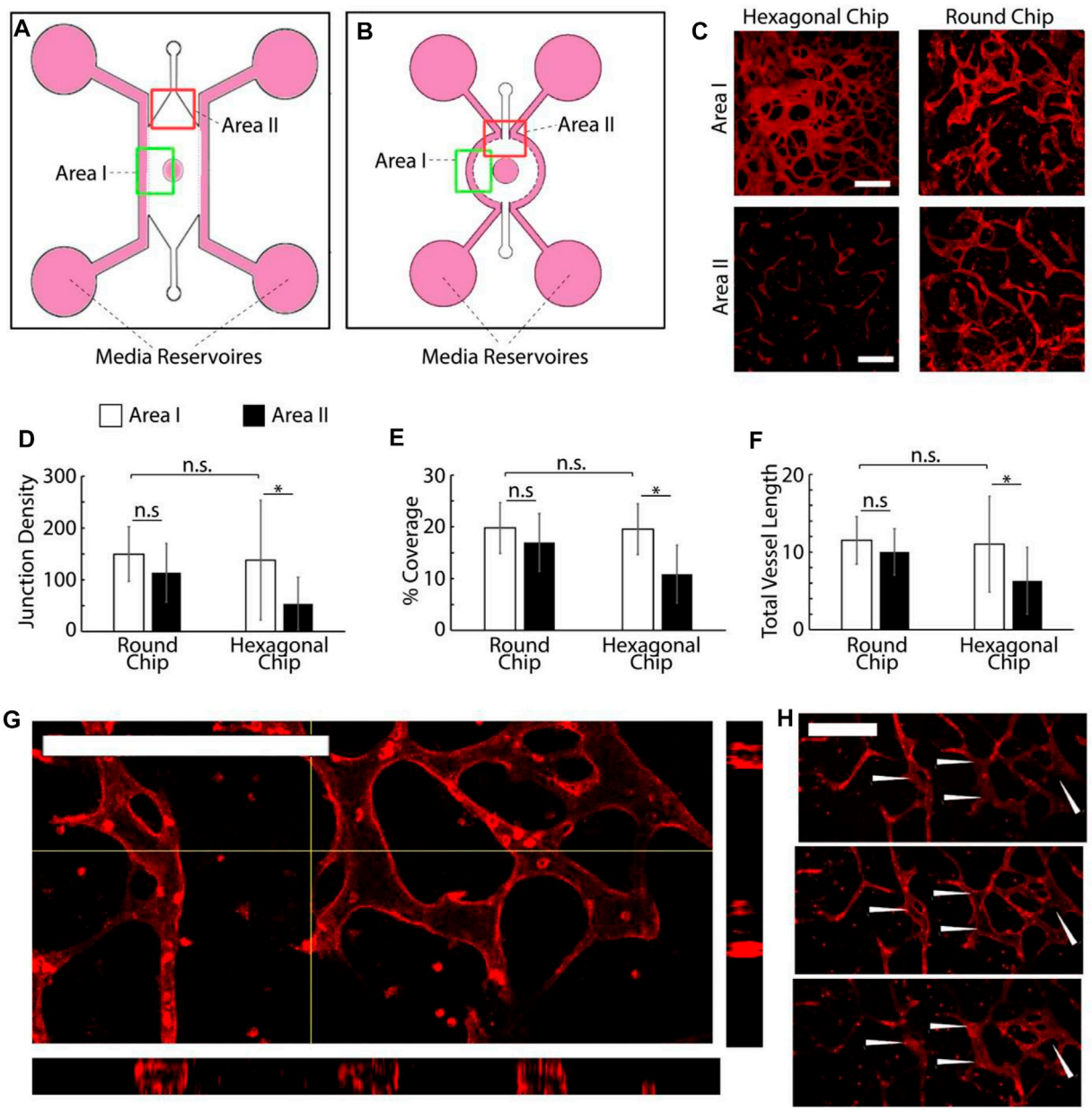

FIGURE 2 | (A,B) Schematic representation of the two chip designs investigated. **(C)** Examples of microvascular networks formed in different areas of the central compartment of hexagonal and round chips. Scale bars: 200 µm. **(D–F)** (D–F) Quantification of the morphology of the corresponding networks. Junction density and total vessel length are expressed in arbitrary units normalised by the section area. **(G–H)** Confocal images of networks formed in round chips displaying luminated structures [**(G)** z-stack projection and cross-section and **(H)** corresponding individual sections taken across one network branch]. *$p < 0.05$; n.s., non-significant, $p > 0.05$; error bars are standard errors; $n = 3$. Scale bars: 200 µm.

Trypsinization was inhibited by the addition of 5 ml trypsin neutralization solution, after which the cells were centrifuged and resuspended in PGM2.

HCA2 fibroblasts—a human telomerase reverse transcriptase (hTERT)-immortalized human dermal fibroblast cell line (Stephens et al., 2004) were cultured in Dulbecco's Modified Eagle Medium (DMEM, Gibco™) supplemented with 10% fetal bovine serum (FBS, Gibco™ 26140079), 1% L-glutamine, and 1% penicillin–streptomycin (PS, Gibco™ 15140122). N/TERT cells (Dickson et al., 2020), a human keratinocyte cell line featuring a constitutive expression of human telomerase reverse transcriptase (hTERT) were cultured in a FAD medium (3:1 DMEM: Ham's F12 Medium) (Thermo Fisher®, 11320074), supplemented with 1% PS, 1% L-glutamine, 10% FBS, 0.5 µg/ml human hydrocortisone (Fisher Scientific®, 35245-0010), 8.47 ng/ml cholera toxin (Sigma-Aldrich®, C8052-1 mg), 10 ng/ml human epidermal growth factor (Peprotech®, AF-100-15), and 5 µg/ml human insulin (Sigma-Aldrich®, 15500).

2.3 Vasculogenesis Assays

A bovine fibrin gel was used as a matrix for vascularization, following protocols reported in the literature (Rohringer et al., 2014). In short, lyophilized bovine fibrinogen (Sigma-Aldrich®, F8630-25G) was dissolved in dPBS to a concentration of 20 mg/ml and filtered to ensure sterility. Separately, a bovine thrombin solution of 4 U/ml was prepared by dissolving lyophilized bovine thrombin derived from bovine plasma (Sigma-Aldrich, T4648-1KU) in 0.1% bovine serum albumin solution (BSA, Sigma-Aldrich, A9418-50G) in dPBS, which was added to EGM-2 to achieve the final concentration. Before injection into the device, 20 µl aliquots of fibrinogen solution were mixed with equal volumes of thrombin solution in which was suspended appropriate densities of HUVECs, which triggered the formation of the final gel encapsulating endothelial cells.

For both chip designs, the wide central chamber was filled with 10 µl of a fibrin gel with a concentration of 10 mg/ml, in which HUVECs were suspended at a density of 6–10 million cells/ml by injection through the 3-mm central well with a cut 20 µl pipette tip. Both side channels were filled with EGM-2 supplemented with 50 ng/ml Vascular Endothelial Growth Factor (VEGF) by filling individual wells at one end of the chip and applying negative pressure to the corresponding well for each channel using a 1,000 µl pipette, therefore allowing channel perfusion. Medium reservoirs were filled equally. Chips were left to incubate at 37°C for approximately 45 min whilst HCA2 cells were passaged and encapsulated in a collagen gel at a density of 2 million cells/ml. The collagen gels were formed using rat tail-derived collagen I, as follows: working over ice, aqueous NaOH (1M) was added to 10X dPBS (ThermoFisher®, 70011044). Rat tail-derived type I collagen (Corning®, 354249) was added to the buffer solution followed by HCA2 cells in dPBS and the mixture was well mixed, resulting in a final collagen concentration of 5 mg/ml and an HCA2 density of 2 million cells/ml. A total of 30 µl of collagen gel solution containing fibroblasts was placed into the central well and allowed to set on the HUVEC-loaded fibrin gel cast at the bottom. Medium wells and the central well were filled with EGM2 containing an additional 50 ng/ml VEGF. The medium was replaced daily and after 1 week of culture was fixed in 4% PFA in PBS and stained for imaging.

2.4 Organotypic Skin-on-a-Chip Formation and Vascularization

2.4.1 Dermal Equivalent Preparation

Fibrin gels were prepared and injected into the vascular compartment of chips, either without cells, at 10^7 cells/ml HUVECs or 10^7 cells/ml HUVECs and 10^6 cells/ml pericytes. A total of 20 µl was injected into each chip. For vascularized chips, devices were filled with EGM-2 containing an additional 50 ng/ml VEGF, which was replaced daily and cultured for 4 days before the addition of the dermal and epidermal equivalents, to allow vascular development. Avascular chips were incubated with VEGF-supplemented EGM2 for 24 h before the addition of the skin equivalent.

For embedding of the dermal equivalent gel precursor, solutions were stored on ice, using pre-cooled pipette tips kept in sterile sealed boxes at 0°C and micro-centrifuge tubes to avoid premature Matrigel® setting. The medium was removed from the reservoirs and central well of the devices. Rat tail-derived collagen I solution of 250 µl high concentration (9 mg/ml) was injected into a micro-centrifuge tube, followed by 100 µl Matrigel® (Corning®, 356234) and 50 µl 10X DMEM (Thermo Fisher®, 11430030). After thorough mixing to ensure homogeneity, the pH was adjusted to 7 by the dropwise addition of sterile 1 M NaOH, in aliquots of 5 µl, followed by further mixing to a volume of approximately 405 µl. A total of 50 µl sterile FBS was added and mixed in, and the mixture was put aside on ice until primary fibroblasts had been passaged and re-suspended to 1 M/ml in complete DMEM. An amount of 50 µl of cell suspension was added to the collagen/Matrigel® mixture and mixed thoroughly to a final fibroblast density of 10^5 cells/ml. An injection of 20 µl of the resulting cell suspension in the gel precursor mixture was made into the central well of the device atop the fibrin scaffold. The injection was carried out on the sides of the well, to avoid the formation of bubbles allowing the matrix to rest evenly across the surface of the fibrin gel underneath and to fill the entire diameter of the well.

2.4.2 Epidermal Equivalent Preparation

Chips were incubated at 37°C for 1 h to allow the gels to set, followed by the passage of N/TERTs by the addition of 10 ml sterile versene solution for 5 min followed by the addition of 2 ml sterile 0.05% trypsin-EDTA for 5 min at 37°C. The cells were re-suspended to 10^6 cells/ml in FAD and 25 µl of the suspension was injected on top of the gel down the side of the central well, to avoid bubble formation. After 10 min of incubation at room temperature to allow N/TERT attachment to the top of the dermal equivalent, the central well and medium wells were filled with FAD and the chips were cultured overnight at 37°C and 5% CO_2. After approximately 18 h of incubation, the medium was aspirated from the chips and fresh FAD medium was replaced, which was done daily over the culture period. The chips were cultured for 7–14 days at 37°C and 5% CO_2 before fixation in 4% PFA.

2.5 Imaging

2.5.1 On-Chip Immunological Staining

For samples that were imaged on-chip, fixation was carried out in 4% PFA in PBS for 15 min, followed by washing with PBS thrice and incubation in 0.2% triton-X for 15 min. Primary and subsequently secondary stains were applied in 3% BSA overnight followed by a PBS wash. The chips were loaded whole into a sample holder mounted to the stage of the Zeiss™ LSM710 confocal microscope and imaged.

2.5.2 Histology

2.5.2.1 Cryo-Histological Sectioning

For sectioning, immunostaining, and confocal imaging, after fixation, the samples were immersed in 30% sucrose solution in PBS overnight by injection into lateral medium wells and the central well. This was aspirated the following day and replaced

with a 10% sucrose/7.5% porcine gelatin solution in PBS and the chips were left at 37°C for 15 min to allow the matrix to set. Simultaneously, some amount of the gelatin solution was carefully pipetted into well plates avoiding bubble formation to a depth of approximately 1 cm, and the plates were left at 4°C for 15 min to allow the matrix to set. Tissues were harvested from the central wells of the chips by slicing the coverslip from the PDMS carefully with a sharp scalpel and cutting chunks from the remaining block until the organotypic was exposed on three sides. At this point, the cultures were scooped from the PDMS and laid atop the set gels in well plates. More gelatin solution was injected to immerse the cultures completely and the well plates were placed back at 4°C for 15 min to set. A cold hexane bath was prepared by dropping pieces of dry ice into hexane in a deep glass dish with thick sides until it reached a temperature of between −30°C and −50°C. Orientation of the blocks was assured by cutting the corners of the blocks to be attached to the sample holder of the cryostat. Samples were frozen, sectioned, and stored at −80°C until ready for staining.

2.5.2.2 Paraffin-Embedded Section De-Waxing and Antigen Unmasking

Redundant human skin was obtained from healthy donors after plastic surgery procedures at the Royal London Hospital or Phoenix Hospital, Essex. All donors provided written informed consent according to local ethical approval (East London Research Ethics Committee, study number 2011-000626-29 and East of England Research Ethics Committee, study number 21/EE/0057). Human skin sections embedded in paraffin wax were dewaxed by incubation at 55°C for 10 min to melt the paraffin followed by immersion in xylenes thrice, each for 15 min. To rehydrate the sections, the slides were left in a bath of ethanol and xylenes at a 1:1 ratio for 5 min, followed by sequential incubation in 100, 95, and 70% ethanol in deionized water, and finally, in pure deionized water (all twice, each for 2 min). To unmask antigens hidden during sample fixation, the deionized water was aspirated and the sections were immersed in a 0.05% trypsin/0.1% $CaCl_2$ solution in deionized water, pre-warmed to 37°C, and were incubated in a humid box for 20 min at 37°C. The samples were washed thrice more with dPBS before staining.

2.5.2.3 Section Staining and Slide Preparation

Before staining, the sections were allowed to equilibrate to room temperature for around 2 h. The sections were outlined with a hydrophobic pen to facilitate staining and reduce the volumes of required reagents. Onto each section, 4% PFA in PBS was dropped for 15 min, followed by a PBS wash, and further 15 min incubation with 0.2% triton-X in PBS. After another PBS wash, the sections were blocked overnight in 3% BSA solution in PBS at 4°C to reduce the risk of dehydration. The sections were incubated with 15 µl primary antibody solution overnight in 3% BSA at 4°C, according to the stain required. These included antibodies with the following antigens: keratin 14 (K14, AbCam® ab192055, 1:250), Involucrin (ThermoFisher®, MA511803, 1:40), Ki67 (RM9106-50, 1:125), laminin-332 (AbCam®, ab14509, 1:250), vimentin (AbCam®, ab8978, 1:150), TGM-1 (SigmaAldrich®, HPA040171, 1:150), and CD31 (BioLegend®, 303126, 1:100). Secondary antibodies were also applied overnight in a 3% BSA solution in PBS frequently alongside rhodamine-phalloidin and DAPI. These were Invitrogen® antibodies purchased from Thermo Fisher® attached to AlexaFluor™ fluorophores with emission wavelengths of 488 nm or 647 nm. Secondary antibodies were raised against antigens according to the animal origins of the primary antibodies and diluted at 1:1,000.

The sections were washed with PBS which was carefully aspirated, followed by the addition of the Fluoromount-G™ Mounting Medium (ThermoFisher®, 00-4,958-02) and a coverslip. Coverslips were allowed to attach at room temperature overnight and the slides were carefully cleaned with ethanol before imaging. Fluorescent imaging was performed with the Zeiss™ LSM710 Confocal microscope.

2.6 Image and Statistical Analysis

For microvessel analysis, Z-stack files were loaded into Fiji and flattened to produce an image across the depth of the microvascularized compartment. These were analyzed in AngioTool (Zudaire et al., 2011) to find the vessel junction number, overall vessel length, and percentage area covered in any given image by the vasculature. To analyze the sections, Z-stacks were taken through the entire depth of the sections and loaded into Fiji. Individual slices were taken from the central image of each stack as the representative of that stack and used for data acquisition and figure production. Statistical analyses were carried out using SPSS by IBM.

3 RESULTS

3.1 Vasculogenesis-on-a-Chip

The proposed design of the microvascularized chip (**Figure 1**) is based on three channel chips previously reported by Kamm et al. (Hernández Vera et al., 2008; Jeon et al., 2014). In these microfluidic systems, three parallel linear channels are separated by micro-posts that can vary significantly in size and shape from one report to another. This enables the central channel to be loaded with an endothelial cell suspension in a gel precursor solution that is allowed to set *in situ* before filling the side channels with tissue culture medium. The device initially selected featured a hexagonal microfluidic chamber, 5 mm wide, with an integrated 3 mm diameter circular central well open to the air, allowing a minimal gap of 1 mm between the circumference of the well and the edge of the chamber. Peripheral medium channels were separated from the central chamber by two parallel series of hexagonal posts, 380 µm long and 90 µm wide, on either side of the microfluidic culture compartment. The morphology and homogeneity of vascular networks formed in such systems were first investigated.

Vascularization was achieved *via* a vasculogenesis protocol adapted from the literature (Kim et al., 2016), consisting of *de novo* capillary formation of HUVECs encapsulated within the fibrin gel in the central compartment. The impact of cell density on vascular network formation was first examined

(**Supplementary Figure S1**). HUVECs were introduced in the central gel compartment at 6, 8, and 10 million cells/ml, as lower cell densities had been previously investigated (Kim et al., 2013). After 7 days of culture, the cells formed interconnected vascular networks that were luminated, as evidenced by confocal microscopy (**Figure 2**). Cell densities had no significant impact on the morphology of the networks formed, within the range tested (**Supplementary Figure S1**). The total cross-section area of the networks, the total length of the capillaries, and their degree of branching were comparable. However, we noted that the quality of the networks differed significantly depending on their position within the channel. Close to the central well (area I), the vascular networks were denser (higher cross-section areas, length, and branching densities) than in the more distant areas, close to the injection channels (area II, **Figures 2D–F**).

To encourage more uniform vascularization, the device was redesigned. The hexagonal microfluidic culture compartment flanked by straight parallel peripheral medium channels was replaced with a round compartment with a circumferential 1 mm wide channel (**Figure 2B**). This design was selected to allow more homogenous distances between the medium channels and the central well. Indeed, the increased distance between the edge of the medium channel and the central well in area II of the hexagonal chips was proposed to lead to differences in homogeneity of the nutrient and oxygen diffusion gradients within the vascular compartment. Hexagonal posts were redesigned to follow the circumference of the central channel. Given the lack of impact of HUVEC density on vascularization, within the range tested, cells were seeded within these redesigned chips at a density of 8 million cells/ml (suspended in 10 mg/ml fibrin gel).

Vascularization surrounding the central channel of the round chips was comparable to the hexagonal chips (**Figures 2C–F**), without significant changes in the vascular network coverage, density, or branching. In contrast to what had been observed with hexagonal chips, a comparison of images taken near the central well of the round chips with those taken near injection channels revealed no significant difference in network architecture either (**Figures 2D–F**). Levels of coverage by vascular networks were comparable near the central well and injection channels, and the associated vascular networks were as dense and branched. This suggests that improved medium diffusion, associated with a more homogenous edge-to-edge distance between medium-supplemented compartments, in a different compartment within the round chips enables the improved formation of homogenous vascular networks. An examination of confocal z-stacks taken of the corresponding vascular compartments also indicated the formation of luminated structures (20 μm of internal diameter) in networks formed in the round chips (**Figures 2G,H**). In turn, we confirmed that these networks were functional and perfusable, *via* an FITC-dextran (70 kDa) assay (**Supplementary Figure S2**). Therefore, our data indicate that round chips support the growth of mature and more homogenous microvascular networks within multi-compartment microfluidic chips. This model was therefore adopted for the development vascularized skin-on-a-chip systems.

3.2 Establishment of a Skin-on-a-Chip Model

To engineer the full-thickness dermal equivalent within our microfluidic model, we proposed to introduce dermal fibroblasts within the central well of round chips. As a first step, we introduced the dermal compartment on top of an acellular fibrin gel, which could subsequently be vascularized, as shown in **Figures 1**, **2**. A collagen I/Matrigel dermal equivalent matrix was selected, based on protocols established for transwell skin equivalent culture (Enjalbert et al., 2020). Fibrin was injected into the microfluidic compartment of the chip and the devices were incubated at 37°C for 5 min, followed by perfusion of the medium channels and filling of all on-chip wells with complete DMEM. The chips were left for 24 h at 37°C to allow bubbles forming at the medium-hydrogel interface to disperse. The medium was then removed from the chips and 20 μl of a dermal equivalent matrix (rat tail-derived collagen I and Matrigel with pH adjusted to 7) together with 10^5 cells/ml primary human dermal fibroblasts were injected in the central well and allowed to set at the surface of the fibrin compartment, for 1 h at 37°C. N/TERT keratinocytes were passaged and resuspended at 1 million cells/ml in the FAD medium, and 25 μl of the suspension was injected on top of the dermal equivalent. Devices were incubated for 10 min at room temperature to facilitate initial N/TERT attachment, followed by the filling of medium wells with the FAD medium. After 24 h incubation, the medium was removed from the chip and replaced. To examine the impact of air-liquid interface culture, which is typically used for the formation of skin equivalents to encourage epidermal stratification and differentiation, dermal equivalents on the chips were either left submerged (fresh FAD introduced into the central well) or exposed to air. The culture was continued for a total of 7 or 14 d, followed by fixation and embedding for histology and immunological staining.

On day 7, the keratinocytes formed confluent epidermal layers across the surfaces of dermal matrices and were positive for basal K14 (**Supplementary Figure S3**). After 14 days of culture, both in submerged conditions and at the air-liquid interface, we observed the formation of confluent stratified epidermal layers, atop the dermal equivalent matrix (**Supplementary Figure S3**). Infrequent proliferative cells (Ki67 positive) were observed in the basal epidermal layers of epidermal equivalents cultured submerged in the medium (**Figure 3**). Although this localization and such overall low rates are typical of skin equivalents and proliferation rates observed *in vivo* (Heenen et al., 1998; Commandeur et al., 2012), the lack of Ki67-positive cells in tissues formed at the air-liquid interfaces was surprising. In agreement with such observations, we also observed significantly thicker epidermal equivalents in submerged cultures (46 ± 16 μm) compared with those formed at the air-liquid interface (24 ± 12 μm, **Figure 3C**). In addition, the abundance of the basement membrane protein laminin-332 was significantly higher in submerged cultures (by a factor of >2 fold, **Figure 3C**), suggesting that keratinocytes in these cultures were also more active at remodeling corresponding interfaces and recreating a normal functional basal lamina.

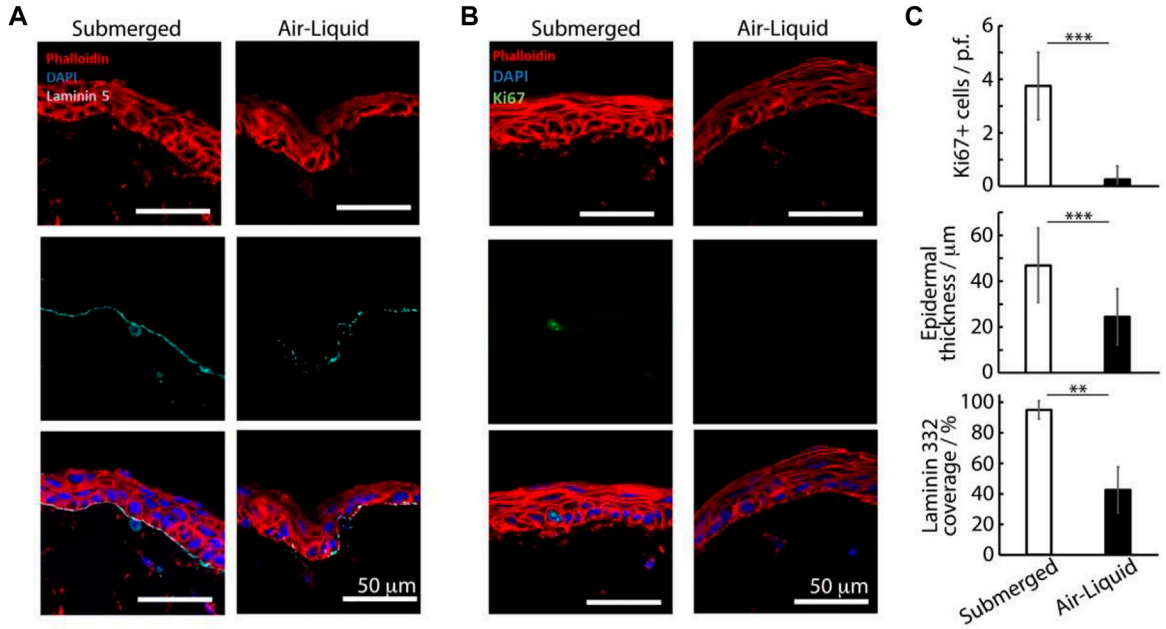

FIGURE 3 | Histology sections of avascular skin-on-chip constructs immuno-stained with phalloidin (red), DAPI (blue), and for laminin 332, **(A)** cyan or Ki67 and **(B)** green. After an initial culture of 7 days, tissues were further cultured for 7 days in submerged or air-liquid conditions. **(C)** Quantification of the corresponding density of Ki67+ cells, epidermal thickness and coverage of laminin 332. $^{**}p < 0.01$; $^{***}p < 0.001$; n.s., non-significant, $p > 0.05$; error bars are standard errors; n = 3.

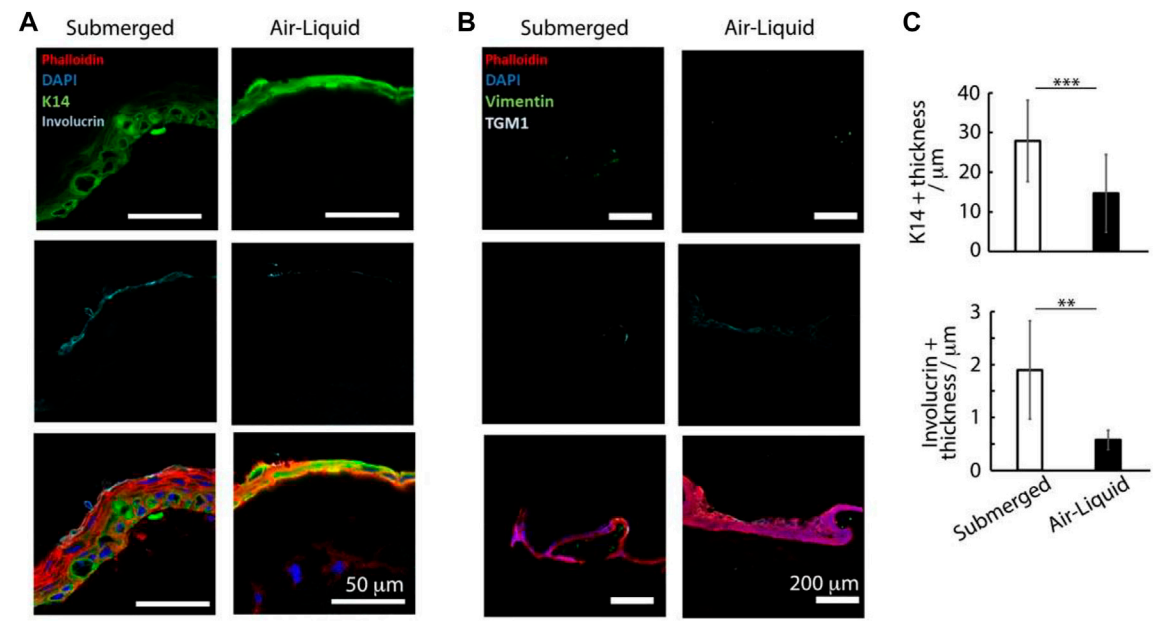

FIGURE 4 | Histology sections of avascular skin-on-chip constructs immuno-stained with phalloidin (red), DAPI (blue), and for K14 and involucrin (green and cyan, respectively); **(A)** for vimentin and transglutaminase green and cyan, respectively. **(B)** After an initial culture of 7 days, tissues were further cultured for 7 days in submerged or air-liquid conditions. **(C)** Quantification of the corresponding density of K14+ tissue thickness and involucrin-positive tissue thickness. $^{**}p < 0.01$; $^{***}p < 0.001$; n.s., non-significant, $p > 0.05$; error bars are standard errors; n = 3.

The thickness of the basal marker keratin 14 was also significantly increased in submerged cultures (28 ± 10 µm) compared with those kept at air-liquid interfaces (15 ± 10 µm, **Figure 4**). Finally, while the expression of the terminal differentiation marker involucrin was observed in the upper-epidermal layers of both cultures, the thickness of the associated

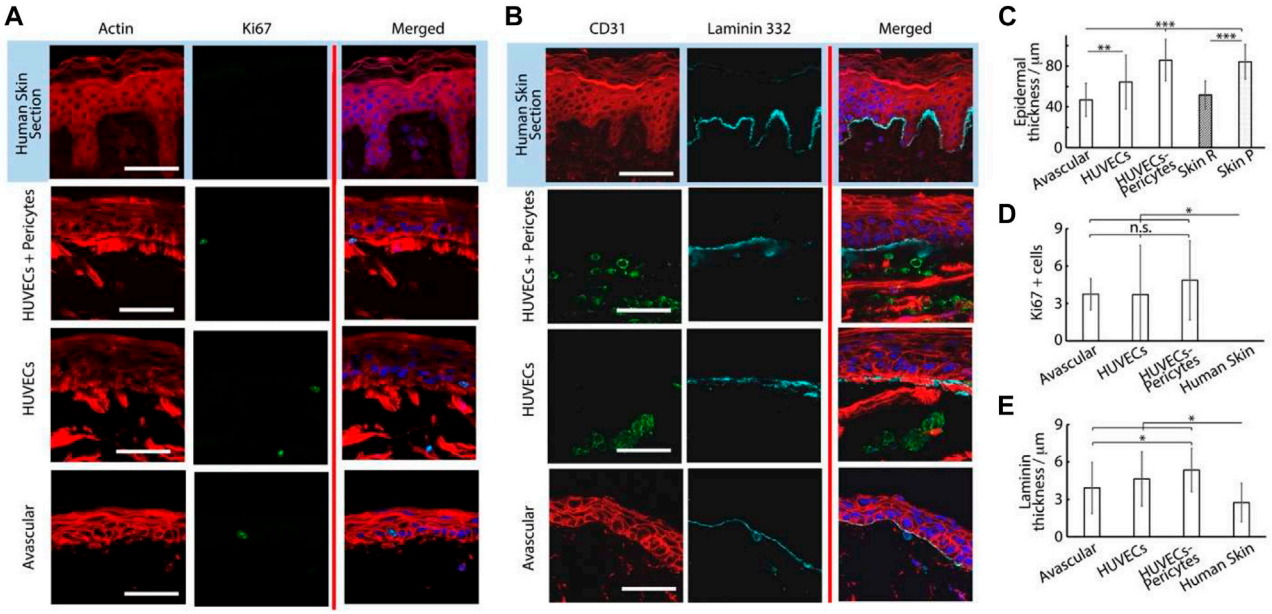

FIGURE 5 | Histology sections of microvascularized skin-on-chip constructs and human skin sections immuno-stained with phalloidin (red), DAPI (blue), and for Ki67, **(A)** green or CD31 and laminin 332 and **(B)** green and cyan, respectively. Tissues were cultured for 14 days in submerged conditions. Scale bars: 50 µm. **(C)** Quantification of the corresponding epidermal thickness, density of Ki67+ cells **(D)** and thickness of laminin 332 **(E)**. $^{*}p < 0.05$; $^{**}p < 0.01$; $^{***}p < 0.001$; n.s., non-significant, $p > 0.05$; error bars are standard errors; n = 3.

differentiated layer was significantly increased in submerged cultures (3.5 ± 2.2 µm) compared with those kept at the air-liquid interface (0.5 ± 0.2 µm, **Figure 4**). We hypothesized that the restricted differentiation and stratification at the air-liquid interfaces was resulting from the reduced nutrient diffusion to epidermal compartments. To improve differentiation and stratification at air-liquid interfaces, we examined the impact of the central well diameter and agitation of the chips (using an orbital shaker, to promote medium transport and flow), but did not observe further maturation of our constructs (**Supplementary Figure S3**). However, a relatively weak expression of the dermal fibroblast marker vimentin was observed in the dermal compartment of both cultures, and very weak staining for the epidermal differentiation marker transglutaminase 1 (TGM-1) was observed in the stratified layers of the corresponding epidermal compartments (**Figure 4B**).

3.3 Microvascularized Skin-on-a-Chip Model

The microvascularized model developed in a fibrin matrix and the stratified human skin equivalent (HSE) were then combined in round chips. In addition, owing to their impact on the maturation and stabilization of microvasculatures (Hirschi and D'amore, 1996; Kim et al., 2013; Campisi et al., 2018), we investigated the impact of pericytes on the resulting vascularized skin equivalents. HUVECs (10^7 cells/ml) were seeded alone or together with human primary pericytes (10^6 cells/ml) in a 10 mg/ml fibrin within the central channel of the round chips. Side channels and the central well were supplemented with an EGM-2 medium containing 50 ng/ml. After 4 days of culture to allow the establishment of a mature microvasculature, the dermal equivalent was introduced into the central well, followed by seeding of N/TERT keratinocytes after 1 h, as previously described. Medium channels and the central well were filled with the FAD medium and the culture was continued for 14 d, under submerged conditions (**Supplementary Figure S4**). Cultures were fixed and dissected from the chips for histological processing and immunological staining. Sections taken from our samples were compared with *ex vivo* human skin sections.

The resulting tissues displayed a well-structured multi-layer epidermal equivalent with flattened stratified squamous cells (**Figure 5**; **Supplementary Figures S5, S6**). Although the overall thickness and level of flattening and stratification of the epidermal compartment remained lower than what can be observed in sections of human skin, the epidermal equivalents were more developed in the presence of microvasculatures (whether with or without pericytes). Rete ridges present *in vivo* in human skin were also not observed in our HSE-chip models, although these are not generally recapitulated in other human skin equivalents reported (Choudhury and Das, 2021). The overall depth of the epidermal compartment significantly increased in vascularized chips (86 ± 20.3 µm, for vascularized chips in the presence of pericytes, compared with 64 ± 26.5 µm, for avascular chips; **Figure 5C**). Although these thicknesses are in line with those reported for skin equivalents (Chopra et al., 2015; Wei et al., 2017), our results indicate that vascularization impacts the establishment of the epidermal structure in skin equivalents.

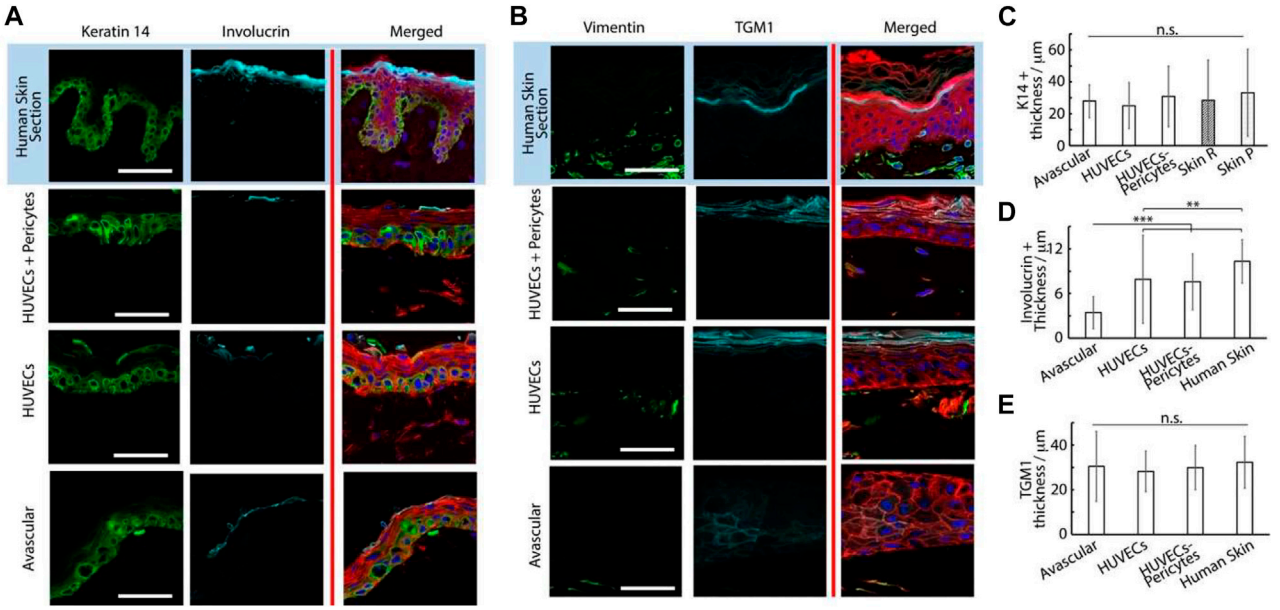

FIGURE 6 | Histology sections of microvascularized skin-on-chip constructs and human skin sections immuno-stained with phalloidin (red), DAPI (blue), and for K14 and involucrin, **(A)** green and cyan, respectively or vimentin and transglutaminase, **(B)** green and cyan, respectively. Tissues were cultured for 14 days in submerged conditions. Scale bars: 50 µm. **(C)** Quantification of the corresponding K14+ tissue thickness , involucrin + tissue thickness **(D)** and transglutaminase + tissue thickness **(E)**. $^{**}p < 0.01$; $^{***}p < 0.001$; n.s., non-significant, $p > 0.05$; error bars are standard errors; n = 3.

To study this phenomenon further, we investigated the stainings of tissue sections. The impact of vascularization on the basal compartment of the epidermal equivalent was relatively modest. We observed a small increase in the thickness of the basement membrane constituent laminin 332 in vascularized chips, compared with avascular models and *ex vivo* skin sections (**Figures 5B,E**). This increase was not statistically significant when comparing avascular and vascularized chips, but *p* values decreased to <0.001 when pericyte/HUVEC vascular networks were used in the vascularized compartment, compared with human skin sections. This modest change in the basement membrane did not translate into differences in the expression of the basal marker keratin 14 (**Figure 6**). Similarly, Ki67-positive cells in the epidermis were confined to the basal layer in all conditions and their frequency was comparable (**Figure 5D**). However, these observations contrasted with the lack of Ki67 expression in the basal compartment of *ex vivo* human skin sections, in line with previous observations made on comparable human sections (Heenen et al., 1998).

Epidermal differentiation marker expression was more established and consistent with the addition of a vascularized dermal compartment: the thickness of involucrin positive layers in chips containing either HUVECs alone or alongside pericytes (8 ± 5.8 and 8 ± 3.8 µm, respectively) compared with avascular models (3 ± 2.2 µm, **Figures 6A,D**). However, involucrin expression remained weaker than in human skin sections (10 ± 2.9 µm). Similarly, staining for transglutaminase was significantly more pronounced in vascularized chips, compared with avascular chips. Beyond expression levels, the localization of transglutaminase was also more obviously localized at the upper layers of the epidermis in vascularized HSE-chips, recapitulating well the pattern of expression typical of human skin sections (**Figure 6B**). We did not observe a significant impact of vascularization on the thickness of transglutaminase expression (**Figure 6E**), but the expression was not confined to the uppermost layers of the epidermal equivalents in avascular chips and could be seen in layers directly above the basal layer.

The impact of vascularization on the dermal compartment could also be clearly observed. CD31 positive structures were obviously only observed in vascularized models, as would be expected from the presence of endothelial cells (**Figure 5B**). Associated with such structures, we clearly observed an increase in vimentin-positive cells in vascularized chips, compared with avascular cultures (**Figure 6B**; **Supplementary Figure S7**). Vimentin-positive cells were clearly denser in human skin histological sections, but this reflects a generally higher degree of cellularity in a normal tissue dermis, compared with the *in vitro* models established.

Further characterization of the vascular compartment was carried out next. We observed extensive dermal microvascular networks spanning the microfluidic compartments underlying the central well cultures of chips loaded with HUVECs alone (bright field images, **Figure 7**), confirmed *via* staining for the endothelial marker CD31 (**Figure 7D**). In the presence of pericytes, vascular networks were also clearly observed, but displayed altered morphologies, in agreement with similar systems reported in the literature (Kim et al., 2015b; Dibble et al., 2022). Pericyte co-cultures displayed reduced total length and branching (**Figures 7A,B**). Such a phenotype is

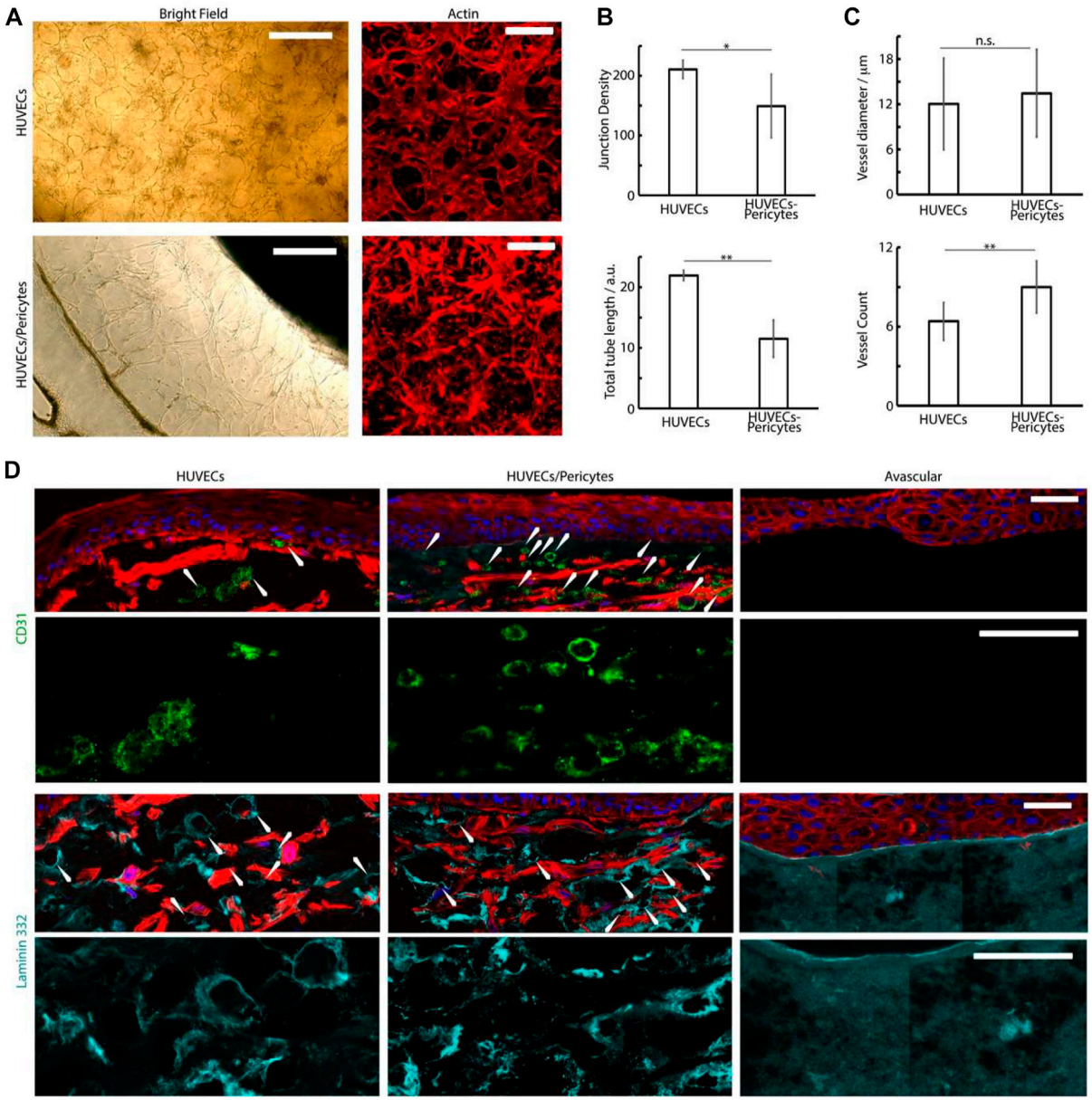

FIGURE 7 | (A) Brightfield and confocal images (phalloidin) of the basal microvascular compartment of chips injected with either HUVECs alone or HUVECs and pericytes, followed by 4 days of culture in EGM2 medium +50 ng/ml VEGF and 2 weeks in FAD medium. Scale bars: 200 µm. **(B,C)** Characterization of the morphology of the corresponding networks. Junction density and total vessel length are expressed in arbitrary units normalised by the section area. **(D)** Histology sections of microvascularized skin-on-chip constructs immuno-stained with phalloidin (red), DAPI (blue), and for CD31 (green) and laminin 332 (cyan). Tissues were cultured for 14 days in submerged conditions. Scale bars: 50 µm. $^{*}p < 0.05$; $^{**}p < 0.01$; n.s., non-significant, $p > 0.05$; error bars are standard errors; n = 3.

proposed to be associated with the maturing and stabilizing role of pericytes, enabling to better retain the stability of resulting networks. Mechanisms involved in this behavior remain unclear, but may involve cytokine secretion (e.g., angiopoietin-1, angiogenin, HGF, TGF-a, and TNF) and perivascular matrix remodeling (Newman et al., 2011). Whilst others reported an impact on endothelial cell-cell junctions (Jeon et al., 2014; Jeon et al., 2015), our previous results did not confirm such effects (Dibble et al., 2022).

To investigate the architecture of the microvasculatures integrated into the dermal equivalents in our cultures, we examined the formation of capillaries in the sections generated (**Figure 7D**). CD31 and laminin stainings clearly established the formation of rosettes associated with the formation of luminated capillaries (**Figure 7D**), in agreement with the recruitment of laminin at the basal membrane of micro-capillaries (Black et al., 1998; Black et al., 1999; Kubota et al., 1988). The density of these structures was clearly increased in HUVEC-pericytes co-cultures,

indicating better retention of the vascular networks within these models (**Figures 7C,D**). The average external diameter of the capillaries determined from the sections, although approximative as only relying on the ability to identify clear transverse sections, were 12 ± 6 μm for monocultures and 13 ± 6 μm for HUVEC/pericytes co-cultures, which correspond to the external diameter of dermal arterial capillaries *in vivo*, identified from human skin sections (Braverman, 2000). Overall, our results are evidencing the supportive role played by pericytes in our model, maintaining the microvasculature integrity despite the use of mixed culture media in our protocol (Hirschi and D'amore, 1996; Campisi et al., 2018; Dibble et al., 2022).

4 DISCUSSION

These data demonstrate that our chip design enables the formation of a microvascular network embedded in a multi-compartment microfluidic system and underlying the formation of a dermal/epidermal skin. The design of a round central chamber and circumferential channels enables the formation of a more homogenous microvasculature within the central compartment (**Figure 2**), in agreement with previous data presented for a vascularized ocular model (Ko et al., 2019b). It is also expected that the circular design selected will result in more homogenous cytokine and growth factor gradients within the different compartments, as was previously described in a model of pluripotent stem cell differentiation (Manfrin et al., 2019) and as briefly discussed in a model of central nervous system axonal growth, across the diameter of a microfluidic compartment (Park et al., 2009).

A surprising result from our study is that skin equivalents, in the absence of a microvasculature, form more mature stratified epidermal compartments under submerged conditions, compared with those cultured at the air-liquid interface. This contrasts with the literature indicating that culture at the air interface, for skin equivalents grown in transwell systems, allows improved stratification and accurate epidermal differentiation marker expression (Prunieras et al., 1983; Rosdy and Clauss, 1990). These results may be explained by the smaller dimensions of the constructs generated and the lower volumes of media required for their culture. Indeed, the smaller dimension may result in higher local oxygen concentrations, impacting keratinocyte commitment and stratification (Ngo et al., 2007). In addition, the smaller volumes may allow greater accumulation of cytokines and growth factors promoting stratification. It may also be that, the lower volumes of media used in the culture at air-liquid interfaces in our chips result in increased cell death, and that the added volume associated with submerged culture helps in limiting such processes, as demonstrated by Lee et al. (2017) in their vascularized skin-on-a-chip. Indeed, tissues formed at the air-liquid interface displayed significantly reduced Ki67 expression, compared with submerged systems (**Figure 3**).

The culture on microvascularized beds further improved the stratification and differentiation of skin equivalents. The use of pericytes was found to have weak but statistically significant impacts on the density of capillaries and their apparent lumination in our skin equivalents (**Figure 7**). Therefore, beyond their initial impact on the morphology of vascular networks, pericytes may contribute to the complementarity of vascularized models with other tissue equivalents, allowing the formation of more complex vascularized tissue models. This may be associated with perivascular matrix remodeling (Bergers and Song, 2005; Avolio et al., 2017) and cytokine secretion, which were found to promote the stability of vascular networks (Sounni et al., 2011; Hurtado-Alvarado et al., 2014).

Improved epidermal stratification and differentiation on the addition of a microvascular component has previously been demonstrated in both *in vivo* mouse and *in vitro* systems (Baltazar et al., 2020). Conversely, Rochon et al. (2009) have shown that various epithelial cell types have a direct impact on endothelial vessel physiology *in vitro*. This is likely due to increased bi-directional diffusion of secreted growth factors and cytokines in the surrounding microenvironment, known to impact differentiation in keratinocyte populations (Ansel et al., 1990; Gröne, 2002). Stromal fibroblasts in the dermal equivalent matrix also likely contribute to the secreted factors to encourage improved epidermal stratification; this has been demonstrated previously in human *in vitro* systems, which commonly report an undifferentiated, unstratified epidermis with a reduced thickness and poor localization of upper-epidermal and basement membrane markers in the absence of proximal fibroblasts (Saintigny et al., 1993). In 2020, Russo et al. (2020) published an extensive review on this topic. Pericytes alongside HUVECs have been shown to increase epidermal thickness and the expression of cytokeratins 1/10 and laminin 332 in *in vitro* skin models, which was also confirmed in engraftment experiments into a murine setting for a duration of 4 weeks (Baltazar et al., 2020). In agreement with this literature, stromal cell interactions are proposed to improve the epidermal architecture in our model.

Overall, our results demonstrate the feasibility of hierarchically structured vascularized-skin-on-chip equivalents, paving the way for the embedding of these systems for therapeutics safety and efficacy testing in a human context *in vitro*. Such models will allow the testing of systemic and topical delivery in realistic scenarios, in platforms that may be compatible with high throughput testing. This still requires the engineering of multi-chip plate systems compatible with high throughput formats, in analogy to some of the epithelial/endothelial tissue models developed on the emulate platforms (Si et al., 2021), and the parallelization of a multi-cellular culture and embedding in the resulting micro-engineered chips. This latter process may require particular attention from the research community as parallelized and automated multi-cell culture systems have not been engineered to date.

DATA AVAILABILITY STATEMENT

The original contributions presented in the study are included in the article/**Supplementary Material**; further inquiries can be directed to the corresponding author.

AUTHOR CONTRIBUTIONS

JEG and JC: conceptualization and project administration. CJ and SC: data curation, formal analysis, validation, visualization, and writing—original draft. JEG and JC: funding acquisition, resources, and supervision. JEG and JC: writing—review and editing, writing—original draft. All authors contributed to the article and approved the submitted version.

FUNDING

This work was funded by the Engineering and Physical Sciences Research Council of UK Research and Innovation (EPSRC grant EP/N50953X/1), the National Centre for the Replacement, Refinement, and Reduction of Animals in Research (NC3Rs, NC/M001636/1, and NC/T2T0319), and the European Research Council (ProLiCell, 772462).

ACKNOWLEDGMENTS

The authors would like to acknowledge the contribution of Atiya Sarmin (Blizard Institute, Whitechapel) for helping to formulate the dermal equivalent used in our model.

SUPPLEMENTARY MATERIAL

The Supplementary Material for this article can be found online at: https://www.frontiersin.org/articles/10.3389/fbioe.2022.915702/full#supplementary-material

REFERENCES

Ackermann, K., Lombardi Borgia, S., Korting, H. C., Mewes, K. R., and Schäfer-Korting, M. (2010). The Phenion Full-Thickness Skin Model for Percutaneous Absorption Testing. *Skin. Pharmacol. Physiol.* 23, 105–112. doi:10.1159/000265681

Ansel, J., Perry, P., Brown, J., Damm, D., Phan, T., Hart, C., et al. (1990). Cytokine Modulation of Keratinocyte Cytokines. *J. Investigative Dermatology.* 94, s101–s107. doi:10.1111/1523-1747.ep12876053

Asbill, C., Kim, N., El-Kattan, A., Creek, K., Wertz, P., and Michniak, B. (2000). Evaluation of a Human Bio-Engineered Skin Equivalent for Drug Permeation Studies. *Pharm. Res.* 17, 1092–1097. doi:10.1023/a:1026405712870

Avolio, E., Alvino, V. V., Ghorbel, M. T., and Campagnolo, P. (2017). Perivascular Cells and Tissue Engineering: Current Applications and Untapped Potential. *Pharmacol. Ther.* 171, 83–92. doi:10.1016/j.pharmthera.2016.11.002

Baish, J. W., Stylianopoulos, T., Lanning, R. M., Kamoun, W. S., Fukumura, D., Munn, L. L., et al. (2011). Scaling Rules for Diffusive Drug Delivery in Tumor and Normal Tissues. *Proc. Natl. Acad. Sci. U.S.A.* 108, 1799–1803. doi:10.1073/pnas.1018154108

Baltazar, T., Merola, J., Catarino, C., Xie, C. B., Kirkiles-Smith, N. C., Lee, V., et al. (2020). Three Dimensional Bioprinting of a Vascularized and Perfusable Skin Graft Using Human Keratinocytes, Fibroblasts, Pericytes, and Endothelial Cells. *Tissue Eng. Part A* 26, 227–238. doi:10.1089/ten.tea.2019.0201

Bellas, E., Seiberg, M., Garlick, J., and Kaplan, D. L. (2012). *In Vitro* 3D Full-Thickness Skin-Equivalent Tissue Model Using Silk and Collagen Biomaterials. *Macromol. Biosci.* 12, 1627–1636. doi:10.1002/mabi.201200262

Bergers, G., and Song, S. (2005). The Role of Pericytes in Blood-Vessel Formation and Maintenance. *Neuro-Oncology* 7, 452–464. doi:10.1215/s1152851705000232

Black, A. F., Hudon, V., Damour, O., Germain, L., Auger, F. A., Gibson, A. L., et al. (1999). A Novel Approach for Studying Angiogenesis: a Human Skin Equivalent with a Capillary-like Network. *Cell. Biol. Toxicol.* 15, 81–90. doi:10.1023/a:1007541713398

Black, A. F., Berthod, F., L'Heureux, N., Germain, L., and Auger, F. A. (1998). *In Vitro* reconstruction of a Human Capillary-like Network in a Tissue-engineered Skin Equivalent. *FASEB J.* 12, 1331–1340. doi:10.1096/fasebj.12.13.1331

Bosch-Fortea, M., Rodriguez-Fraticelli, A. E., Herranz, G., Hachimi, M., Barea, M. D., Young, J., et al. (2019). Micropattern-based Platform as a Physiologically Relevant Model to Study Epithelial Morphogenesis and Nephrotoxicity. *Biomaterials* 218, 119339. doi:10.1016/j.biomaterials.2019.119339

Braverman, I. M. (2000). The Cutaneous Microcirculation. *J. Investigative Dermatology Symposium Proc.* 5, 3–9. doi:10.1046/j.1087-0024.2000.00010.x

Campisi, M., Shin, Y., Osaki, T., Hajal, C., Chiono, V., and Kamm, R. D. (2018). 3D Self-Organized Microvascular Model of the Human Blood-Brain Barrier with Endothelial Cells, Pericytes and Astrocytes. *Biomaterials* 180, 117–129. doi:10.1016/j.biomaterials.2018.07.014

Chen, C. S., Mrksich, M., Huang, S., Whitesides, G. M., and Ingber, D. E. (1997). Geometric Control of Cell Life and Death. *Science* 276, 1425–1428. doi:10.1126/science.276.5317.1425

Chen, M. B., Whisler, J. A., Fröse, J., Yu, C., Shin, Y., and Kamm, R. D. (2017). On-chip Human Microvasculature Assay for Visualization and Quantification of Tumor Cell Extravasation Dynamics. *Nat. Protoc.* 12, 865–880. doi:10.1038/nprot.2017.018

Chopra, K., Calva, D., Sosin, M., Tadisina, K. K., Banda, A., De La Cruz, C., et al. (2015). A Comprehensive Examination of Topographic Thickness of Skin in the Human Face. *Aesthet. Surg. J.* 35, 1007–1013. doi:10.1093/asj/sjv079

Choudhury, S., and Das, A. (2021). Advances in Generation of Three-Dimensional Skin Equivalents: Pre-clinical Studies to Clinical Therapies. *Cytotherapy* 23, 1–9. doi:10.1016/j.jcyt.2020.10.001

Colton, C. (1995). Implantable Biohybrid Artificial Organs. *Cell. Transplant.* 4, 415–436. doi:10.1016/0963-6897(95)00025-s

Commandeur, S., Van Drongelen, V., De Gruijl, F. R., and El Ghalbzouri, A. (2012). Epidermal Growth Factor Receptor Activation and Inhibition in 3Din Vitromodels of Normal Skin and Human Cutaneous Squamous Cell Carcinoma. *Cancer Sci.* 103, 2120–2126. doi:10.1111/cas.12026

Connelly, J. T., Gautrot, J. E., Trappmann, B., Tan, D. W.-M., Donati, G., Huck, W. T. S., et al. (2010). Actin and Serum Response Factor Transduce Physical Cues from the Microenvironment to Regulate Epidermal Stem Cell Fate Decisions. *Nat. Cell. Biol.* 12, 711–718. doi:10.1038/ncb2074

Costa, P., Gautrot, J. E., and Connelly, J. T. (2014). Directing Cell Migration Using Micropatterned and Dynamically Adhesive Polymer Brushes. *Acta Biomater.* 10, 2415–2422. doi:10.1016/j.actbio.2014.01.029

Dibble, M., Di Cio, S., Luo, P., Balkwill, F., and Gautrot, J. E. (2022). Impact of Pericytes on the Stabilisation of Microvascular Networks in Microfluidic Systems in Response to Nanotoxicity. BioRxiv. doi:10.1101/2022.05.03.490457

Dickson, M. A., Hahn, W. C., Ino, Y., Ronfard, V., Wu, J. Y., Weinberg, R. A., et al. (2020). Human Keratinocytes that Express hTERT and also Bypass a p16INK4a-Enforced Mechanism that Limits Life Span Become Immortal yet Retain Normal Growth and Differentiation Characteristics. *Mol. Cell. Biol.* 20 (4), 1436–1447.

Enjalbert, F., Dewan, P., Caley, M. P., Jones, E. M., Morse, M. A., Kelsell, D. P., et al. (2020). 3D Model of Harlequin Ichthyosis Reveals Inflammatory Therapeutic Targets. *J. Clin. Investig.* 130, 4798–4810. doi:10.1172/jci132987

Galie, P. A., Nguyen, D.-H. T., Choi, C. K., Cohen, D. M., Janmey, P. A., and Chen, C. S. (2014). Fluid Shear Stress Threshold Regulates Angiogenic Sprouting. *Proc. Natl. Acad. Sci. U.S.A.* 111, 7968–7973. doi:10.1073/pnas.1310842111

Gautrot, J. E., Wang, C., Liu, X., Goldie, S. J., Trappmann, B., Huck, W. T. S., et al. (2012). Mimicking Normal Tissue Architecture and Perturbation in Cancer with Engineered Micro-epidermis. *Biomaterials* 33, 5221–5229. doi:10.1016/j.biomaterials.2012.04.009

Gröne, A. (2002). Keratinocytes and Cytokines. *Veterinary Immunol. Immunopathol.* 88, 1–12. doi:10.1016/s0165-2427(02)00136-8

Hassell, B. A., Goyal, G., Lee, E., Sontheimer-Phelps, A., Levy, O., Chen, C. S., et al. (2017). Human Organ Chip Models Recapitulate Orthotopic Lung Cancer Growth, Therapeutic Responses, and Tumor Dormancy *In Vitro*. *Cell. Rep.* 21, 508–516. doi:10.1016/j.celrep.2017.09.043

Heenen, M., Thiriar, S., Noël, J.-C., and Galand, P. (1998). Ki-67 Immunostaining of Normal Human Epidermis: Comparison with 3H-Thymidine Labelling and PCNA Immunostaining. *Dermatology* 197, 123–126. doi:10.1159/000017982

Helmlinger, G., Yuan, F., Dellian, M., Jain, R. K., Dellian, M., and Jain, R. K. (1997). Interstitial pH and pO2 Gradients in Solid Tumors *In Vivo*: High-Resolution Measurements Reveal a Lack of Correlation. *Nat. Med.* 3, 177–182. doi:10.1038/nm0297-177

Hernández Vera, R., Genové, E., Alvarez, L., Borrós, S., Kamm, R., Lauffenburger, D., et al. (2008). Interstitial Fluid Flow Intensity Modulates Endothelial Sprouting in Restricted Src-Activated Cell Clusters during Capillary Morphogenesis. *Tissue Eng. Part A* 15, 175–185.

Hirschi, K., and D'amore, P. A. (1996). Pericytes in the Microvasculature. *Cardiovasc. Res.* 32, 687–698. doi:10.1016/0008-6363(96)00063-6

Homan, K. A., Gupta, N., Kroll, K. T., Kolesky, D. B., Skylar-Scott, M., Miyoshi, T., et al. (2019). Flow-enhanced Vascularization and Maturation of Kidney Organoids *In Vitro*. *Nat. Methods.* 16, 255–262. doi:10.1038/s41592-019-0325-y

Huh, D., Matthews, B. D., Mammoto, A., Montoya-Zavala, M., Hsin, H. Y., and Ingber, D. E. (2010). Reconstituting Organ-Level Lung Functions on a Chip. *Science* 328, 1662–1668. doi:10.1126/science.1188302

Hurtado-Alvarado, G., Cabañas-Morales, A. M., and Gómez-Gónzalez, B. (2014). Pericytes: Brain-Immune Interface Modulators. *Front. Integr. Neurosci.* 7, 80. doi:10.3389/fnint.2013.00080

Jenkins, G. (2013). Rapid Prototyping of PDMS Devices Using SU-8 Lithography. *Microfluid. Diagnostics Methods Protoc.* 949, 153–168. doi:10.1007/978-1-62703-134-9_11

Jeon, J. S., Bersini, S., Gilardi, M., Dubini, G., Charest, J. L., Moretti, M., et al. (2015). Human 3D Vascularized Organotypic Microfluidic Assays to Study Breast Cancer Cell Extravasation. *Proc. Natl. Acad. Sci. U.S.A.* 112, 214–219. doi:10.1073/pnas.1417115112

Jeon, J. S., Bersini, S., Whisler, J. A., Chen, M. B., Dubini, G., Charest, J. L., et al. (2014). Generation of 3D Functional Microvascular Networks with Human Mesenchymal Stem Cells in Microfluidic Systems. *Integr. Biol.* 6, 555–563. doi:10.1039/c3ib40267c

Kilic, O., Pamies, D., Lavell, E., Schiapparelli, P., Feng, Y., Hartung, T., et al. (2016). Brain-on-a-chip Model Enables Analysis of Human Neuronal Differentiation and Chemotaxis. *Lab. Chip.* 16, 4152–4162. doi:10.1039/c6lc00946h

Kim, B. S., Gao, G., Kim, J. Y., and Cho, D. W. (2019). 3D Cell Printing of Perfusable Vascularized Human Skin Equivalent Composed of Epidermis, Dermis, and Hypodermis for Better Structural Recapitulation of Native Skin. *Adv. Healthc. Mater.* 8, e1801019–11. doi:10.1002/adhm.201801019

Kim, C., Kasuya, J., Jeon, J., Chung, S., and Kamm, R. D. (2015a). A Quantitative Microfluidic Angiogenesis Screen for Studying Anti-angiogenic Therapeutic Drugs. *Lab. Chip.* 15, 301–310. doi:10.1039/c4lc00866a

Kim, H. J., and Ingber, D. E. (2013). Gut-on-a-chip Microenvironment Induces Human Intestinal Cells to Undergo Villus Differentiation. *Integr. Biol.* 5, 1130–1140. doi:10.1039/c3ib40126j

Kim, J., Chung, M., Kim, S., Jo, D. H., Kim, J. H., and Jeon, N. L. (2015b). Engineering of a Biomimetic Pericyte-Covered 3D Microvascular Network. *PLoS One.* 10, e0133880. doi:10.1371/journal.pone.0133880

Kim, S., Chung, M., Ahn, J., Lee, S., and Jeon, N. L. (2016). Interstitial Flow Regulates the Angiogenic Response and Phenotype of Endothelial Cells in a 3D Culture Model. *Lab. Chip.* 16, 4189–4199. doi:10.1039/c6lc00910g

Kim, S., Lee, H., Chung, M., and Jeon, N. L. (2013). Engineering of Functional, Perfusable 3D Microvascular Networks on a Chip. *Lab. Chip.* 13, 1489–1500. doi:10.1039/c3lc41320a

Ko, J., Lee, Y., Lee, S., Lee, S. R., and Jeon, N. L. (2019b). Human Ocular Angiogenesis-Inspired Vascular Models on an Injection-Molded Microfluidic Chip. *Adv. Healthc. Mater* 8, e1900328–10. doi:10.1002/adhm.201900328

Ko, J., Ahn, J., Kim, S., Lee, Y., Lee, J., Park, D., et al. (2019a). Tumor Spheroid-On-A-Chip: a Standardized Microfluidic Culture Platform for Investigating Tumor Angiogenesis. *Lab. Chip.* 19, 2822–2833. doi:10.1039/c9lc00140a

Kubota, Y., Kleinman, H. K., Martin, G. R., and Lawley, T. J. (1988). Role of Laminin and Basement Membrane in the Morphological Differentiation of Human Endothelial Cells into Capillary-like Structures. *J. Cell. Biol.* 107, 1589–1598. doi:10.1083/jcb.107.4.1589

Kwak, B. S., Jin, S. P., Kim, S. J., Kim, E. J., Chung, J. H., and Sung, J. H. (2020). Microfluidic Skin Chip with Vasculature for Recapitulating the Immune Response of the Skin Tissue. *Biotechnol. Bioeng.* 117, 1853–1863. doi:10.1002/bit.27320

Lancaster, M. A., Renner, M., Martin, C.-A., Wenzel, D., Bicknell, L. S., Hurles, M. E., et al. (2013). Cerebral Organoids Model Human Brain Development and Microcephaly. *Nature* 501, 373–379. doi:10.1038/nature12517

Langan, E. A., Philpott, M. P., Kloepper, J. E., and Paus, R. (2015). Human Hair Follicle Organ Culture: Theory, Application and Perspectives. *Exp. Dermatol.* 24, 903–911. doi:10.1111/exd.12836

Lee, J., Rabbani, C. C., Gao, H., Steinhart, M. R., Woodruff, B. M., Pflum, Z. E., et al. (2020). Hair-bearing Human Skin Generated Entirely from Pluripotent Stem Cells. *Nature* 582, 399–404. doi:10.1038/s41586-020-2352-3

Lee, S., Jin, S.-P., Kim, Y. K., Sung, G. Y., Chung, J. H., and Sung, J. H. (2017). Construction of 3D Multicellular Microfluidic Chip for an *In Vitro* Skin Model. *Biomed. Microdevices.* 19, 22. doi:10.1007/s10544-017-0156-5

Li, L., Fukunaga-Kalabis, M., and Herlyn, M. (2011). The Three-Dimensional Human Skin Reconstruct Model: a Tool to Study Normal Skin and Melanoma Progression. *J. Vis. Exp.* 12, 1–5. doi:10.3791/2937

Liu, J., Long, H., Zeuschner, D., Räder, A. F. B., Polacheck, W. J., Kessler, H., et al. (2021). Synthetic Extracellular Matrices with Tailored Adhesiveness and Degradability Support Lumen Formation during Angiogenic Sprouting. *Nat. Commun.* 12, 3402. doi:10.1038/s41467-021-23644-5

Liu, Y., Suwa, F., Wang, X., Takemura, A., Fang, Y. R., Li, Y., et al. (2007). Reconstruction of a Tissue-Engineered Skin Containing Melanocytes. *Cell. Biol. Int.* 31, 985–990. doi:10.1016/j.cellbi.2007.03.009

Loskill, P., Hardwick, R. N., and Roth, A. (2021). Challenging the Pipeline. *Stem Cell. Rep.* 16, 2033–2037. doi:10.1016/j.stemcr.2021.08.004

Manfrin, A., Tabata, Y., Paquet, E. R., Vuaridel, A. R., Rivest, F. R., Naef, F., et al. (2019). Engineered Signaling Centers for the Spatially Controlled Patterning of Human Pluripotent Stem Cells. *Nat. Methods.* 16, 640–648. doi:10.1038/s41592-019-0455-2

Mazlyzam, A. L., Aminuddin, B. S., Fuzina, N. H., Norhayati, M. M., Fauziah, O., Isa, M. R., et al. (2007). Reconstruction of Living Bilayer Human Skin Equivalent Utilizing Human Fibrin as a Scaffold. *Burns* 33, 355–363. doi:10.1016/j.burns.2006.08.022

Menon, N. V., Tay, H. M., Wee, S. N., Li, K. H. H., and Hou, H. W. (2017). Micro-engineered Perfusable 3D Vasculatures for Cardiovascular Diseases. *Lab. Chip.* 17, 2960–2968. doi:10.1039/c7lc00607a

Nelson, C. M., Vanduijn, M. M., Inman, J. L., Fletcher, D. A., and Bissell, M. J. (2006). Tissue Geometry Determines Sites of Mammary Branching Morphogenesis in Organotypic Cultures. *Science* 314, 298–300. doi:10.1126/science.1131000

Newman, A. C., Nakatsu, M. N., Chou, W., Gershon, P. D., and Hughes, C. C. W. (2011). The Requirement for Fibroblasts in Angiogenesis: Fibroblast-Derived Matrix Proteins Are Essential for Endothelial Cell Lumen Formation. *MBoC* 22, 3791–3800. doi:10.1091/mbc.e11-05-0393

Ngo, M. A., Sinitsyna, N. N., Qin, Q., and Rice, R. H. (2007). Oxygen-dependent Differentiation of Human Keratinocytes. *J. Investigative Dermatology.* 127, 354–361. doi:10.1038/sj.jid.5700522

Park, J., Koito, H., Li, J., and Han, A. (2009). Microfluidic Compartmentalized Co-culture Platform for CNS Axon Myelination Research. *Biomed. Microdevices.* 11, 1145–1153. doi:10.1007/s10544-009-9331-7

Polacheck, W. J., German, A. E., Mammoto, A., Ingber, D. E., and Kamm, R. D. (2014). Mechanotransduction of Fluid Stresses Governs 3D Cell Migration. *Proc. Natl. Acad. Sci. U.S.A.* 111, 2447–2452. doi:10.1073/pnas.1316848111

Pruniéras, M., Régnier, M., and Woodley, D. (1983). Methods for Cultivation of Keratinocytes with an Air-Liquid Interface. *J. Investig. Dermatol.* 81, 28s–33s. doi:10.1111/1523-1747.ep12540324

Rochon, M. H., Fradette, J., Fortin, V., Tomasetig, F., Roberge, C. J., Baker, K., et al. (2009). Normal Human Epithelial Cells Regulate the Size and Morphology of Tissue-Engineered Capillaries. *Tissue Eng. Part A* 16, 1457–1468. doi:10.1089/ten.tea.2009.0090

Rohringer, S., Hofbauer, P., Schneider, K. H., Husa, A. M., Feichtinger, G., Peterbauer-Scherb, A., et al. (2014). Mechanisms of Vasculogenesis in 3D Fibrin Matrices Mediated by the Interaction of Adipose-Derived Stem Cells and Endothelial Cells. *Angiogenesis* 17 (4), 921–933.

Ronaldson-Bouchard, K., Ma, S. P., Yeager, K., Chen, T., Song, L., Sirabella, D., et al. (2018). Advanced Maturation of Human Cardiac Tissue Grown from Pluripotent Stem Cells. *Nature* 556, 239–243. doi:10.1038/s41586-018-0016-3

Rosdy, M., and Clauss, L.-C. (1990). Terminal Epidermal Differentiation of Human Keratinocytes Grown in Chemically Defined Medium on Inert Filter Substrates at the Air-Liquid Interface. *J. Investigative Dermatology.* 95, 409–414. doi:10.1111/1523-1747.ep12555510

Ruiz, S. A., and Chen, C. S. (2008). Emergence of Patterned Stem Cell Differentiation within Multicellular Structures. *Stem Cells.* 26, 2921–2927. doi:10.1634/stemcells.2008-0432

Russo, B., Brembilla, N. C., and Chizzolini, C. (2020). Interplay between Keratinocytes and Fibroblasts: A Systematic Review Providing a New Angle for Understanding Skin Fibrotic Disorders. *Front. Immunol.* 11, 648. doi:10.3389/fimmu.2020.00648

Saintigny, G., Bonnard, M., Damour, O., and Collombel, C. (1993). Reconstruction of Epidermis on a Chitosan Cross-Linked Collagen-GAG Lattice: Effect of Fibroblasts. *Acta Derm. Venereol.* 73, 175–180. doi:10.2340/0001555573175180

Sakar, M. S., Eyckmans, J., Pieters, R., Eberli, D., Nelson, B. J., and Chen, C. S. (2016). Cellular Forces and Matrix Assembly Coordinate Fibrous Tissue Repair. *Nat. Commun.* 7, 11036. doi:10.1038/ncomms11036

Shahabeddin, L., Berthod, F., Damour, O., and Collombel, C. (1990). Characterization of Skin Reconstructed on a Chitosan-Cross-Linked Collagen-Glycosaminoglycan Matrix. *Skin. Pharmacol. Physiol.* 3, 107–114. doi:10.1159/000210857

Shin, N., Kim, Y., Ko, J., Choi, S. W., Hyung, S., Lee, S. E., et al. (2021). Vascularization of iNSC Spheroid in a 3D Spheroid-on-a-chip Platform Enhances Neural Maturation. *Biotech Bioeng.* 119, 566–574. doi:10.1002/bit.27978

Si, L., Bai, H., Rodas, M., Cao, W., Oh, C. Y., Jiang, A., et al. (2021). A Human-Airway-On-A-Chip for the Rapid Identification of Candidate Antiviral Therapeutics and Prophylactics. *Nat. Biomed. Eng.* 5, 815–829. doi:10.1038/s41551-021-00718-9

Sobrino, A., Phan, D. T. T., Datta, R., Wang, X., Hachey, S. J., Romero-López, M., et al. (2016). 3D Microtumors *In Vitro* Supported by Perfused Vascular Networks. *Sci. Rep.* 6, 31589. doi:10.1038/srep31589

Sounni, N. E., Paye, A., Host, L., and Noël, A. (2011). MT-MMPS as Regulators of Vessel Stability Associated with Angiogenesis. *Front. Pharmacol.* 2, 111. doi:10.3389/fphar.2011.00111

Stark, H.-J., Boehnke, K., Mirancea, N., Willhauck, M. J., Pavesio, A., Fusenig, N. E., et al. (2006). Epidermal Homeostasis in Long-Term Scaffold-Enforced Skin Equivalents. *J. Investigative Dermatology Symposium Proc.* 11, 93–105. doi:10.1038/sj.jidsymp.5650015

Stephens, P., Grenard, P., Aeschlimann, P., Langley, M., Blain, E., Errington, R., et al. (2004). Crosslinking and G-Protein Functions of Transglutaminase 2 Contribute Differentially to Fibroblast Wound Healing Responses. *J. Cell. Sci.* 117, 3389–3403. doi:10.1242/jcs.01188

Tan, K. Y., Lin, H., Ramstedt, M., Watt, F. M., Huck, W. T. S., and Gautrot, J. E. (2013). Decoupling Geometrical and Chemical Cues Directing Epidermal Stem Cell Fate on Polymer Brush-Based Cell Micro-patterns. *Integr. Biol.* 5, 899–910. doi:10.1039/c3ib40026c

Trappmann, B., Baker, B. M., Polacheck, W. J., Choi, C. K., Burdick, J. A., and Chen, C. S. (2017). Matrix Degradability Controls Multicellularity of 3D Cell Migration. *Nat. Commun.* 8, 371. doi:10.1038/s41467-017-00418-6

Watt, F. M., Jordan, P. W., and O'neill, C. H. (1988). Cell Shape Controls Terminal Differentiation of Human Epidermal Keratinocytes. *Proc. Natl. Acad. Sci. U.S.A.* 85, 5576–5580. doi:10.1073/pnas.85.15.5576

Wei, J. C. J., Edwards, G. A., Martin, D. J., Huang, H., Crichton, M. L., and Kendall, M. a. F. (2017). Allometric Scaling of Skin Thickness, Elasticity, Viscoelasticity to Mass for Micro-medical Device Translation: From Mice, Rats, Rabbits, Pigs to Humans. *Sci. Rep.* 7, 15885. doi:10.1038/s41598-017-15830-7

Wufuer, M., Lee, G., Hur, W., Jeon, B., Kim, B. J., Choi, T. H., et al. (2016). Skin-on-a-chip Model Simulating Inflammation, Edema and Drug-Based Treatment. *Sci. Rep.* 6, 37471. doi:10.1038/srep37471

Zudaire, E., Gambardella, L., Kurcz, C., and Vermeren, S. (2011). A Computational Tool for Quantitative Analysis of Vascular Networks. *PloS one* 6 (11), e27385.

Conflict of Interest: The authors declare that the research was conducted in the absence of any commercial or financial relationships that could be construed as a potential conflict of interest.

Publisher's Note: All claims expressed in this article are solely those of the authors and do not necessarily represent those of their affiliated organizations, or those of the publisher, the editors, and the reviewers. Any product that may be evaluated in this article, or claim that may be made by its manufacturer, is not guaranteed or endorsed by the publisher.